Ring-Resonator Based Widely-Tunable Narrow-Linewidth Si/InP Integrated Lasers

Minh A. Tran, Duanni Huang, Joel Guo, Tin Komljenovic, Paul A. Morton, and John E. Bowers

(Invited Paper)

***Abstract*—This paper presents recent results on widely-tunable narrow-linewidth semiconductor lasers using a ring-resonator based mirror as the extended cavity. Two generations of lasers on the heterogeneous Si/InP photonic platform are presented. The first-generation lasers, with a total footprint smaller than 0.81 mm^2, showed an intrinsic linewidth of ∼2 kHz over a 40 nm wavelength tuning range across C+L bands. The second-generation lasers using ultra-low loss silicon waveguides and a novel cavity design achieved an intrinsic linewidth below 220 Hz. The lasers also possess an ultrawide wavelength tuning range of 110 nm across three optical communication bands (S+C+L). These are records among all fully integrated semiconductor lasers reported in the literature.**

***Index Terms*—Semiconductor lasers, tunable lasers, optical ring-resonators, ultra-low noise.**

I. Introduction

LOW noise, widely tunable lasers, with spectral linewidth of kHz level or lower, are in demand by an increasing number of applications, such as coherent communications, LiDAR, optical sensing and spectroscopy [1]–[5]. Such low noise is only commercially available in solid-state lasers, fiber-based lasers and blazed-gratings or fibers based external cavity lasers. Thus, these lasers tend to be bulky, expensive and not scalable for mass production. Semiconductor diode lasers, although attractive for their low form factor, mass producibility and compatibility to integrated circuits, intrinsically have low coherence with typical linewidth in the 100 kHz range or worse.

It is well known that the linewidth of semiconductor lasers can be narrowed by utilizing an external cavity [6]–[8]. With proper design, the external cavity can provide both wavelength tunability and linewidth reduction. Many types of external cavity lasers have been commercialized with outstanding performance such as blazed grating lasers [9], high Q whispering resonator lasers [10], and fiber Bragg grating lasers [11] among others. In recent years, with the advance in integrated silicon photonics, there has been a great interest in external cavity lasers formed by assembling a passive photonics chip as an external cavity to a gain chip. This hybrid approach is attractive because it allows for the gain chip and external cavity to be separately optimized. External cavities based on planar light wave circuits (PLC) [12], low loss silicon nitride [13]–[15], and silicon [16], [17] have been demonstrated. The drawback regarding these assembled hybrid semiconductor lasers is their limited scalability, as each laser must be individually assembled. Alignment between the chips is critical, which slows down the process and increases cost. Furthermore, many of the applications listed above require that the lasers are resistant to vibration and shock. This is another reason why a fully integrated solution is preferred over hybrid solutions, as environmental factors can impact the coupling between the two chips.

Heterogeneous silicon photonics enables the possibility to integrate extended cavity lasers on a single chip. Heterogeneous integration on silicon involves the wafer bonding of unprocessed materials on a wafer level scale, providing a clear path towards scaling and high-volume production [18]. The resulting devices also lie on the same chip. Similar to hybrid integration, heterogeneous integration also has the benefit of selecting the best material to perform each function (i.e., lasers, low-loss waveguides, detectors) to form highly complex photonic integrated circuits (PIC) [19]. Thus, heterogeneously integrated lasers possess all the scaling benefits of monolithic integration while obtaining greater flexibility in material selection, which can lead to superior laser noise performance.

In this paper, we present the architecture, design and characterization of widely tunable lasers on silicon. The key to these lasers is the designs of the mirrors, using multiple ring resonators, as well as heterogeneous integration of InP on silicon. The ring resonator-based mirror simultaneously provides the tuning mechanism of the laser as well as the linewidth reduction [20], [21]. The first generation of these lasers use standard rib silicon waveguides with typical loss ∼1.2 dB/cm to achieve >40 nm tuning span and linewidth in the single kHz range. In the second generation, a novel design utilizing ultra-low loss silicon waveguides [22] to form large, high-Q ring resonators

Manuscript received June 6, 2019; revised August 5, 2019; accepted August 6, 2019. Date of publication August 19, 2019; date of current version September 9, 2019. This work was supported in part by DARPA MTO DODOS under Contract HR0011-15-C-055 and in part by Morton Photonics DARPA MTO STTR program under Contract W911NF-16-C-0072. The work of D. Huang was supported by the National Science Foundation Graduate Research Fellowship Program. *(Corresponding author: Minh A. Tran.)*

M. A. Tran, D. Huang, J. Guo, T. Komljenovic, and J. E. Bowers are with the Department of Electrical and Computer Engineering, University of California Santa Barbara, Santa Barbara, CA 93106-9010 USA (e-mail: minhtran@ece.ucsb.edu; duanni@umail.ucsb.edu; joelguo@ucsb.edu; tkomljenovic@ece.ucsb.edu; bowers@ece.ucsb.edu).

P. A. Morton is with Morton Photonics, West Friendship, MD 21794 USA (e-mail: pmorton@mortonphotonics.com).

Color versions of one or more of the figures in this article are available online at http://ieeexplore.ieee.org.

Digital Object Identifier 10.1109/JSTQE.2019.2935274

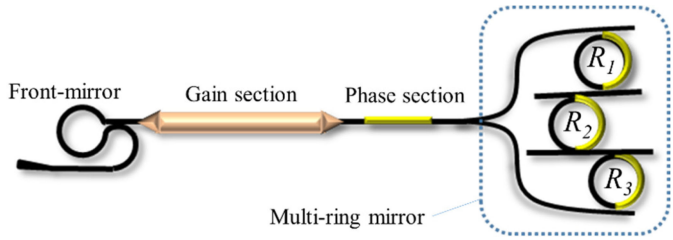

Fig. 1. Schematic structure of a basic widely tunable Si/III-V laser based on multiring mirrors. Here, the three ring resonators are used to illustrate the multiring mirror structure, in which add-drop rings are cascaded within a loop.

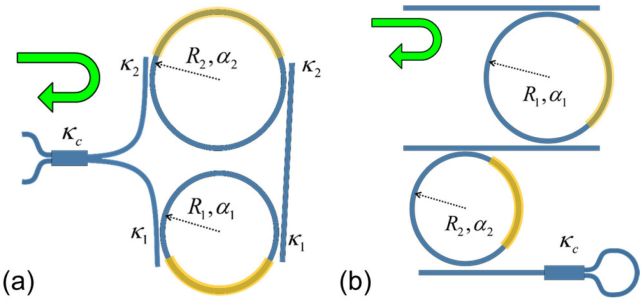

Fig. 2. Typical configuration of a) multi-rings within a loop mirror b) multi-rings separated from a loop mirror. Here we only show dual-ring configurations as an example, but the number of ring resonators can be larger.

[23], [24] is used to demonstrate lasers with a wavelength tuning range of 110 nm and ultra-low phase noise (<220 Hz linewidth). The term "linewidth" throughout this paper, if not specified otherwise, refers to the quantum noise limited Lorentzian linewidth (also called "fundamental", "intrinsic" or "Schawlow-Townes" linewidth) characterized from a frequency noise measurement [25].

The organization of the paper is as follows. In Section II, we describe the laser architecture and then explain the principles of wavelength tuning and linewidth reduction. In the next section, we present the details of the design, fabrication and the results achieved on the two generations of tunable lasers. We conclude the paper with discussion on future directions for further improving the laser performance.

II. Ring-Resonator Based Tunable Laser Theory

A. Laser Architecture

The generic configuration of lasers throughout this work is shown in Fig. 1, involving the following components.

Front mirror (low reflectivity mirror): The front-side (output) mirror is formed by a Sagnac-type loop mirror. The reflectivity of the mirror is determined by the coupling strength of the coupler.

Optical amplifier Si/InP waveguide (gain section): The gain section consists of a silicon rib waveguide etched 231 nm out of 500 nm, with bonded III-V material on top. The Si width in the amplifier is chosen to be 850 nm which balances out the low internal loss and high gain requirements for the laser. Three InAlGaAs quantum wells are used in the gain material [26]. The length of this active element can be varied depending on the lengths and losses of other components in the laser. Transitions from the optical amplifier Si/InP waveguides to passive Si waveguide are realized with a taper structure detailed in [26], [27] with typical loss of -0.5 dB per transition and lower than -33 dB reflection.

Phase section: A metal strip is deposited vertically on the top of the oxide cladding of the Si waveguide, forming the microheater for phase tuning using the thermo-refractive effect. This is used to tune the cavity modes of the laser.

Multi-ring resonant mirror: The back-side mirror of the laser is a reflector formed by multiple ring resonators, with thermal phase tuners on each ring to enable spectral alignment. This tuning mechanism is preferred over other methods using carrier injection or depletion because it is simple to implement and more importantly it does not affect the waveguide loss. This reflector serves as a single wavelength filter for the laser, and its design is the focus of the following sections.

B. Wavelength Tuning

A ring-resonator mirror refers to a structure in which one or multiple rings are cascaded in add-drop configuration. The rings can be placed inside a loop mirror, as in Fig. 2a, or a separate loop mirror can added to the end in Fig. 2b. The former is used in the lasers in this work, while the latter is more commonly found in lasers consisting of separate gain and passive chips. In each case, the loop of the structures can be formed by a 2×2 or 1×2 waveguide couplers. Broadband and/or tunable couplers are preferred to maintain the 50:50 splitting ratio across the operational wavelength range. Within this loop, ring resonators with slightly different radii are cascaded to shape the Vernier spectrum needed for wavelength tuning. The Vernier free spectral range (FSR) formed by two ring resonators is determined by Equation (1), where FSR_m is FSR of the m^{th} ring.

$$FSR_{Vernier} = \frac{FSR_1 \cdot FSR_2}{|FSR_1 - FSR_2|} \tag{1}$$

$$FSR_m = \frac{\lambda^2}{2\pi R_m n_g} \tag{2}$$

Here, the cross-coupling ratios for each ring, ring radius and amplitude propagation loss constant are denoted by κ_m, R_m, α_m ($m = 1, 2$). Assuming symmetric coupling for each ring, *i.e.*, coupling ratios to the two bus waveguides are the same, the complex amplitude reflectivity of the mirror is given by the following equations:

$$r_{mirror} = -2j\sqrt{(1-\kappa_c^2)\,\kappa_c^2} \cdot \prod_m t_{drop}\left(\kappa_m, \kappa_m, R_m, \alpha_m\right) \tag{3}$$

$$t_{drop}\left(\kappa_m, \kappa_m, R_m, \alpha_m\right) = \frac{-\kappa_m^2 (2\pi R_m \alpha_m)^{1/2} e^{j2\pi R_m \beta_p/2}}{1-(1-\kappa_m^2)\,2\pi R_m \alpha_m e^{j2\pi R_m \beta_p}} \tag{4}$$

As an example, the spectral responses of the dual-ring mirror reflection with ring-bus power coupling ratios $\kappa_1 = \kappa_2 = 0.125$

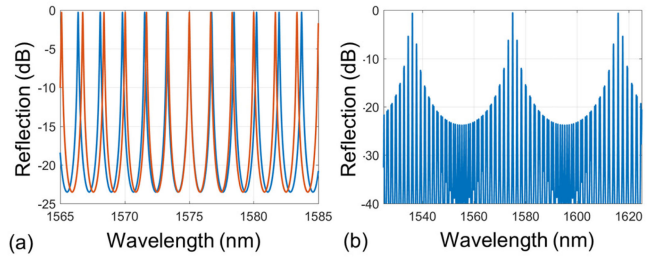

Fig. 3. (a) Reflection spectra of individual rings (b) Combined spectrum of the dual-ring mirror. Dispersion is neglected for simplicity.

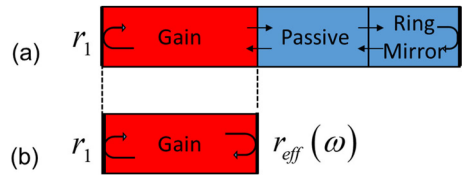

Fig. 4. Modeling of the dual-ring mirror laser for steady-state analysis (a) Block diagram representation of the laser sections (b) Equivalent cavity with effective mirror to model the extended passive sections.

are calculated using (3) and (4). Fig. 3a shows the individual spectra of the rings with several-nm FSR. The synthesized spectral response of the dual-ring mirror, Fig. 3b, shows a much broader FSR. This Vernier FSR sets the range for the wavelength tuning of our lasers. Heaters are used to tune the individual resonances of the rings. The heaters can either be controlled together for continuous wavelength tuning within a single ring's FSR, or controlled individually for discrete wavelength tuning, stepping by a single ring's FSR.

C. Spectral Linewidth Narrowing

The lasers can be modelled as a three-section laser shown in Fig. 4a. Following the effective mirror model, the laser is simplified in Fig. 4b. Here, the gain section (formed by heterogeneous Si/III-V waveguide) and the front mirror can be lumped into a single active section on the left-hand-side with the reflection coefficient r_1. The phase section and silicon waveguides used for routing are lumped into the passive section, connecting to the ring mirror on the right-hand-side. As the reflection on the active-passive transition is low [26], it is neglected in our analysis.

Next, we replace all the passive sections in Fig. 4a by an effective mirror with complex wavelength dependence represented by $r_{eff}(\omega)$. This substitution is valid since we are looking for steady-state solutions in this analysis [28]. The effective reflectivity is the product of transfer functions of all passive parts and the active-passive transition, given by Equation (5).

$$r_{eff}(\omega) = t^2_{transition}(\omega) \cdot t^2_{passive}(\omega) \cdot r_{mirror}(\omega) \quad (5)$$

Here, $t_{transition}(\omega)$ is simply an attenuation constant representing the transmission loss at the active-passive transition, which is equivalent to -1 dB (or $\sim$80%) on average over the C+L bands accounting for two tapers on both ends of the Si/III-V amplifier waveguide. For a total length L_p of about 1 mm accounted for all passive waveguide routing and phase section, the transfer function for the passive waveguides is given by Equation (6), where α_p and β_p are respectively the waveguide electric field propagation loss and the effective propagation constant in the silicon waveguide:

$$t_{passive}(\omega) = \exp(-\alpha_p L_p - j\beta_p L_p) \quad (6)$$

The last term for the dual-ring mirror reflection $r_{mirror}(\omega)$ has been expressed in (3) previously. To study the laser linewidth, we use the formalism carried out by Patzak et al. in [29] and Kazarinov and Henry in [30]. Due to the frequency dependence of the phase and reflectivity of the extended passive section in Equations (4) and (6) and Fig. 3b, the linewidth of the otherwise solitary Fabry-Perot laser is reduced by a factor F^2 where $F = 1+A+B$. Analytical calculation of the Lorentzian linewidth of our laser is carried out following the equations below:

$$\Delta\nu = \frac{\Delta\nu_0}{F^2} = \frac{\Delta\nu_0}{(1+A+B)^2} \quad (7)$$

$$A = \frac{1}{\tau_0}\mathrm{Re}\left\{j\frac{d\ln r_{eff}(\omega)}{d\omega}\right\} = \frac{1}{\tau_0}\frac{d\varphi_{eff}}{d\omega} \quad (8)$$

$$B = -\frac{\alpha_H}{\tau_0}\mathrm{Im}\left\{j\frac{d\ln r_{eff}(\omega)}{d\omega}\right\} = \frac{\alpha_H}{\tau_0}\frac{d\ln|r_{eff}(\omega)|}{d\omega} \quad (9)$$

$$\Delta\nu_0 = \frac{1}{4\pi}\frac{v_g h\nu n_{sp}\alpha_{tot}\alpha_m}{P_0\left[1+\frac{r_1}{|r_{eff}(\omega)|}\frac{1-|r_{eff}(\omega)|^2}{1-r_1^2}\right]}\left(1+\alpha_H^2\right) \quad (10)$$

The effective mirror term $r_{eff}(\omega)$ can be separated into effective amplitude and phase parts as $r_{eff}(\omega) = |r_{eff}(\omega)|\exp(-j\varphi(\omega))$. The real part, amplitude factor $r_0(\omega)$, represents the field feedback from the extended passive section to the gain section; $\tau_0 = \frac{2n_g L_a}{c}$ is the photon round-trip time in the active section. In Equation (7), $\Delta\nu_0$ represents the Schawlow-Townes linewidth of a solitary Fabry-Perot diode laser with mirror reflectivities r_1 and $|r_{eff}(\omega)|$. As output power P_0 from the laser is collected on the low reflective side (r_1), the equation for $\Delta\nu_0$ is given by (10) where $v_g$is the group effective index, h is the Planck constant, ν is the lasing frequency, n_{sp} is the spontaneous emission factor, $\alpha_{tot} = \alpha_i + \alpha_m$is the total loss, $\alpha_m = -\frac{1}{L_a}\ln(r_1|r_{eff}(\omega)|)$ is the mirror loss and α_i is the internal loss of the active section.

Let us discuss the physical meanings of these factors and equations to obtain some intuitive understanding of the mechanisms for linewidth narrowing phenomena involved.

First, the factor A reflects the increase in roundtrip accumulated phase – equivalent to the effective cavity length enhancement mainly provided by the ring resonances in our case. An increase in the factor A means the passive length of the laser cavity becomes longer, hence the total volume occupied by photon in the laser cavity is effectively enlarged. In contrast, the carrier occupied volume *i.e.*, the volume of active layer (typically quantum wells or quantum dots, is unchanged. The ratio between the total carrier volume to the total photon volume is defined as confinement factor parameter. By enlarging the

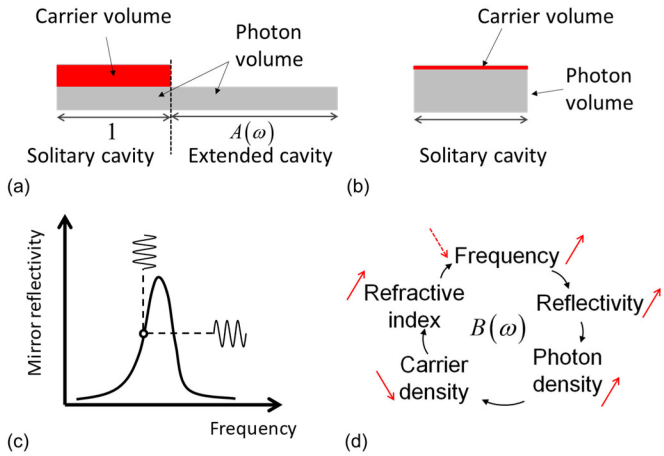

Fig. 5. (a) Illustration of the role of factor A in lowering laser confinement factor in longitudinal orientation (b) Lowering the confinement factor on transversal orientation (c-d) Illustrative explanation of the detuned loading (or optical negative feedback) effect provided by a dispersive mirror.

total photon volume via an increase in *A* using extended cavity, we basically lower the net confinement factor by reducing the confinement factor in the longitudinal direction (length along the cavity), as illustrated in Fig. 5a. One should note the term "volume" in this context refers to the optical mode volume – not the physically occupied by the said layers. Since spontaneous emission events only happen within the carrier occupied volume, lower confinement factor results in lower rate of a spontaneous emission coupling into the lasing mode, hence, lower noise. That is the so-called noise dilution mechanism for lowering the linewidth, here achieved by leveraging the magnitude of the factor *A*.

It is worth noting that another design strategy is to lower the net confinement factor in transversal orientation, as illustrated in Fig. 5b. By lowering the physical volume of active layer (*e.g.*, number of quantum-well layers) and/or lowering the optical mode confinement of the active layer to the transversal mode, one can effectively reduce the net confinement factor. In the Si/III-V heterogeneous waveguide system, lowering the confinement factor comes with the benefit of lower internal loss, as loss in silicon is typically much lower than III-V claddings. This allows for a high-Q cavity in a seemingly solitary laser configuration. Good results using this high coherent laser concept have been demonstrated by Santis et al. [31], [32].

On the other hand, the factor *B* represents the magnitude of the optical negative feedback effect [30] (also known as detuned loading [33]), that helps stabilize the laser frequency via the phase-amplitude coupling of the lasing field – a unique phenomenon in semiconductor lasers characterized by the linewidth enhancement factor α_H. As illustrated in Fig. 5c and d where the mirror reflectivity is a resonant function of the optical frequency. When the lasing frequency is at the marked point (*i.e.*, the positive slope side), an increase in laser frequency increases the reflectivity, leads to the increase of the photon density in the cavity, and hence decreases carrier density, which in turn causes the frequency to decrease due to the carrier plasma effect. This negative feedback loop helps stabilize the laser frequency, hence lower the laser frequency noise. In contrast, if the lasing occurs on the other side of the mirror resonant peak (*i.e.*, negative slope side), a positive feedback loop is formed with which frequency noise is amplified and linewidth is broadened.

Since the strength of the negative feedback effect is dependent on the strength of the coupling between carrier density and optical frequency via the carrier plasma effect, factor *B* is proportional to the linewidth enhancement factor α_H [34], the very factor that accounts for the broadening of the linewidth in solitary lasers. In other words, the detuned loading effect diminishes the role of factor α_H in the frequency noise of an extended cavity laser. This phenomenon makes integrated extended cavity lasers almost reliance-free onα_H; that is a significant advantage compared to solitary lasers in which the linewidth scales with $(1+\alpha_H^2)$.

To end this section, we combine all equations from (7) to (10) to derive the full form of the linewidth for extended cavity laser in Equation (11) shown at the bottom of the next page. As can be clearly seen, both nominator and denominator parts in (11) contain α_H^2 term, signifying the meaning of the two aforementioned physical processes involved in linewidth of extended cavity lasers.

III. Laser Demonstrations

In this section, we will present the details of our achievement of the two generations of tunable lasers heterogeneously integrated on silicon based on the multi-ring mirror architecture in Fig. 1. The first-generation (Gen. 1) lasers, with kHz-level spectral linewidth, were built upon the standard process-design-kit for the heterogeneous Si/InP developed at UCSB. The second-generation (Gen. 2) lasers with the inclusion of ultra-low loss waveguides reached down to hundreds-Hz level linewidth. The design parameters for the design and simulation of two laser generations are listed in Table I. Detailed reasonings for these design parameters is explained in the text that follows.

A. Generation 1: kHz Level Spectral Linewidth Lasers

For this first generation of tunable lasers, a rib waveguide etched 231 nm out of 500 nm is used for the resonators. Thermal oxide serves as the bottom buried oxide (BOX) while the top cladding is deposited with PECVD oxide. Both cladding layers are 1 μm thick to minimize substrate leakage and loss due to the metal heaters, which are put on the top of the waveguide for phase tuning.

The waveguide loss is measured to be to be 1.2 dB/cm and 1.0 dB/cm at 1550 nm for quasi single-mode waveguides with widths of 650 nm and 800 nm. For the ring resonators, we have chosen 650 nm as the waveguide width. Wider waveguides will have less propagation loss, but lower power coupling into the resonator for a given gap between the ring and the bus waveguide. The ring radii of the Vernier rings are chosen to be larger than 60 μm, for which bending loss can be neglected.

1) Gen.1 Laser Design and Fabrication: The configuration of the laser (Fig. 6) follows the architecture described previously. In this particular design, the front-side mirror formed by looping

TABLE I
LIST OF LASER DESIGN PARAMETERS FOR TWO LASER GENERATIONS

Symbol	Description	Gen. 1	Gen. 2
λ	Wavelength	1.575 µm	
h	Planck constant	6.626e-34 m^2kg/s	
c	Light velocity	299792458 m/s	
ν	Optical frequency	190.344 THz	
v_g	Modal group velocity	c / n_g	
n_{sp}	Population inversion factor	1.6	
α_H	Linewidth enhancement factor	4.0	
α_i	Gain section internal loss	6 cm^{-1}	
n_g	Modal group index	3.689	**3.608**
α_p	Si waveguide loss	1.2 dB/cm	**0.16 dB/cm**
d	III-V/Si taper loss	0.5 dB	0.5 dB
L_a	Gain length	1000 µm	**2500 µm**
L_p	Passive routing length	1000 µm	**2000 µm**
R_1	Ring 1 radius	60 µm	**599.97 µm**
R_2	Ring 2 radius	62.5 µm	**600.86 µm**
R_3	Ring 3 radius	-	**707.57 µm**
$\kappa_1^2=\kappa_2^2=\kappa_3^2$	Ring power coupling coefficient	0.125	**0.09**

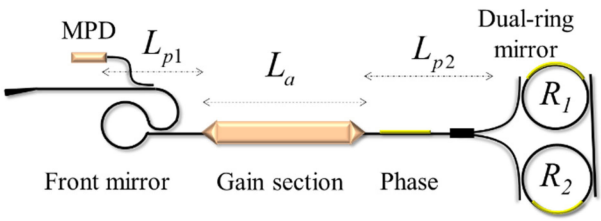

Fig. 6. Schematic structure of a dual-ring mirror-based laser. The front-mirror is a loop mirror formed with a bent-straight coupler. Gain section is an optical amplifier heterogeneous Si/III-V waveguide, bridged to the Si passive waveguides via two Si/III-V tapers. The phase tuner is a microheater on the top cladding of the Si waveguide. The back-mirror is a multiring mirror with two ring resonators of radii R_1 and R_2 and 3-dB multimode interferometer (MMI) coupler. There are also microheaters on the ring resonators for tuning the resonances.

the two ports of a bent-straight coupler has a designed ~40–50% power reflectivity. The length of the laser gain section is 1 mm and a MMI coupler was used to tap out 15% from the front side to a photodiode for on-chip monitoring.

Design parameters necessary for laser analysis were listed in Table I. The estimated values of the three parameters A, B, F as functions of frequency detuning from the lasing wavelength (1575 nm) are shown in Fig. 7a. Based on that, the Lorentzian linewidth is then estimated using Equation 11. The calculation result plotted in Fig. 7b shows that at ring resonance, the linewidth is about 5 kHz. A slight detuning of the frequency to the lower side reduces the linewidth down to the minimum level of about 2 kHz.

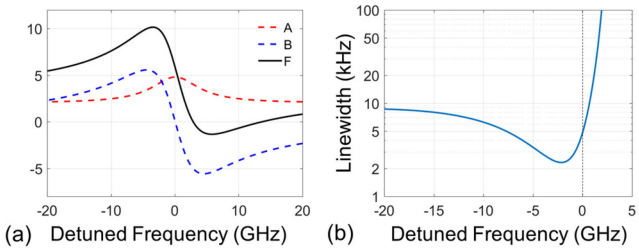

Fig. 7. (a) Calculated values for coefficients A, B and F (a) estimated Lorentzian linewidth as functions of frequency detuned from the dual-ring mirror's resonance frequency assuming an output power of 10 mW. Values of parameters used for these calculations are listed in Table I.

The designed laser is then fabricated in a standard Si/InP heterogeneous process [35], [36]. Scanning electron microscopic images of the dual-ring mirror after silicon etching, a photo of the bonded wafer after InP substrate removal, and another SEM image of the Si/III-V taper (details can be found in [27]) after InP mesa etching are shown in Fig. 8a-c. A completed laser has a footprint of about 2.7 × 0.3 mm^2 as shown in Fig. 8d. The angled facets of the lasers were mechanically polished to couple to a lensed fiber.

2) Gen. 1 Laser Characterization: The laser was measured on a temperature-controlled stage set at 20°C. The output light is coupled into a 2.5 μm spot-size lensed fiber for characterization of spectral properties such as wavelength tuning, spectral linewidth and frequency noise. A Faraday based in-line optical isolator with larger than 50 dB extinction ratio was used immediately after the laser to eliminate any unintentional reflections towards the laser.

The light-current-voltage (L-I-V) curve of the laser was measured by ramping up the injection current while both heaters on the rings are off. The lasing wavelength is stable near 1565 nm under these conditions. For each current value, the power applied to phase section heater of the laser was tuned to maximize the output power based on the tap signal received at the monitor photodiode. This aligns the longitudinal mode of the laser with the peak reflectivity formed by the Vernier rings, and results in the smooth, kink-free L-I curve in Fig. 9. The output power was measured using a broad-area photodetector. The plots shown in Fig. 9 shows a threshold current of about 33 mA.

a) Gen. 1 laser wavelength tuning: We characterized the laser wavelength tuning characteristics at a fixed injection current of 120 mA (~4x threshold current) to the gain section of the laser. A coarse wavelength sweep was first performed to acquire the lasing spectra across the tuning range, as shown in Fig. 10. The spectra show stable single mode lasing across a 40 nm tuning range with side-mode suppression ratio (SMSR) larger than 50 dB.

Next, a full two-dimensional sweep of the ring tuners is carried out to achieve the tuning map for the laser. In our test procedure,

$$\Delta\nu = \frac{1}{4\pi}\frac{v_g h\nu n_{sp}\alpha_{tot}\alpha_m}{P_0\left[1+\frac{r_1}{|r_{eff}(\omega)|}\frac{1-|r_{eff}(\omega)|^2}{1-r_1^2}\right]}\frac{\left(1+\alpha_H^2\right)}{\left(1+\frac{\alpha_H}{\tau_0}\frac{d\ln|r_{eff}(\omega)|}{d\omega}+\frac{1}{\tau_0}\frac{d\varphi_{eff}}{d\omega}\right)^2} \quad (11)$$

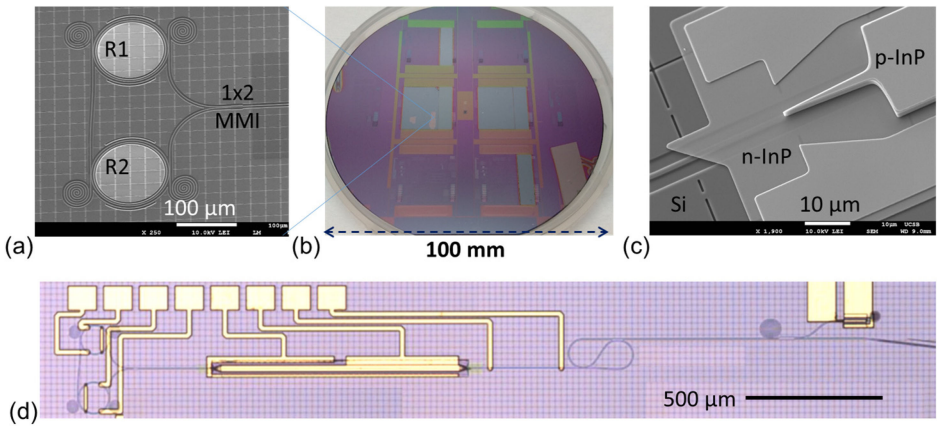

Fig. 8. (a) An SEM image of the dual-ring mirror on silicon (b) The patterned SOI wafers with bonded InP materials after substrate removal (c) An SEM image of the Si/III-V taper for the active-passive transition (d) Microscopic image of the fabricated laser. A photodiode at the end of a tap-out coupler is used to monitor the output power from the laser and to assist the wavelength tuning.

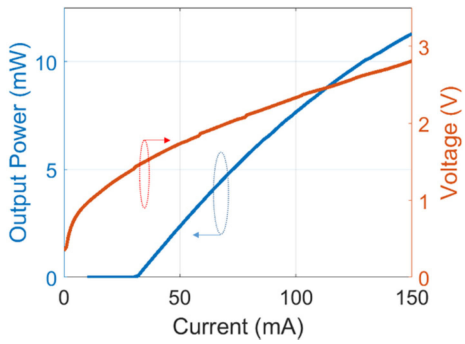

Fig. 9. L-I-V curve of the dual-ring laser with lasing wavelength of 1565 nm.

the electrical power applied to the heaters on top of two ring resonators are stepped by equal amounts. For each operation point, the power applied to the phase heater is optimized to achieve the maximum output power, and the resulting laser wavelength is recorded. The procedure is automated using the monitor photodiode as real-time feedback. A linear and smooth tuning map was obtained as shown in Fig. 10.

The corresponding side-mode suppression ratio (SMSR) map is plotted in Fig. 10. SMSRs on almost all of lasing points are within the range 45∼55 dB. The variation on the SMSR originates from how well the two ring spectra are aligned to each other at the pre-determined heater setpoints in the test. Some outlier operation points with very low SMSRs correspond to multimode lasing that happens when the two ring spectra are exactly misaligned, and two modes are simultaneously able to lase. This is not a problem in the real operation of the laser, in which the two rings would be tuned continuously to avoid such situations. Multimode lasing is also more common at the edges of the tuning range, which can be mitigated by increasing the Vernier FSR beyond the targeted tuning range of the laser.

We took a closer look into the wavelength tuning characteristics of our laser in two tuning schemes: Fine tuning scheme is done using the heater on the phase section, and the coarse tuning scheme is done using the heaters on ring resonators. In Fig. 11a, the lasing wavelength is continuously red-shifted when we ramped up the heater power to the phase section while keeping heaters on rings fixed. The continuous tune ranges about 0.25 nm before the lasing mode hops to the adjacent longitudinal mode on the blue side. The jump step is measured to be 66 pm, which is the laser's longitudinal mode spacing at the rings' resonance. Furthermore, we can tune the ring resonators to achieve coarse tunability by stepping across the ring's individual resonances (Fig. 11b). The step of 1.7 nm is exactly equal to the FSR of ring resonator of 60 μm radius shown in Fig. 3. The good match between these two key parameters means the specifications (on the group index and the power coupling ratio of the ring-bus couplers) of fabricated devices are close to the designed values.

b) Gen. 1 laser frequency noise and Lorentzian linewidth: All modeling and analysis on the laser linewidth reported here is solely focused on the quantum noise limited Lorentzian linewidth. An accurate measurement of the laser's true Lorentzian linewidth is of paramount importance if we want to have relevant measured data to validate the theoretical analysis above. Unfortunately, the measurement with the commonly used delayed self-heterodyne method [37] suffers from the existence of colored noises, *e.g.*, flicker noise (*1/f*) inherent to semiconductor devices, which significantly broadens the shape of the beat note spectrum [38]. Furthermore, it is difficult to isolate the test setup from electromagnetic interference, especially for an unpackaged laser being tested in the lab environment. For these reasons, we characterized the Lorentzian linewidth of our laser by measuring its frequency noise spectrum, using a commercial noise measurement system (OEWaves) [39]. The intrinsic linewidth, or Lorentzian linewidth of the laser can then be extracted by analyzing the frequency noise at higher frequencies where the measurement is relatively free from technical noise from electronics, vibrations, and other environmental factors.

Fig. 12a shows a typical one-sided power spectral density of the laser frequency fluctuation as a function of frequency of the fabricated laser, taken at 120 mA pump current and slightly detuned from the peak resonance of 1576 nm wavelength. *1/f*

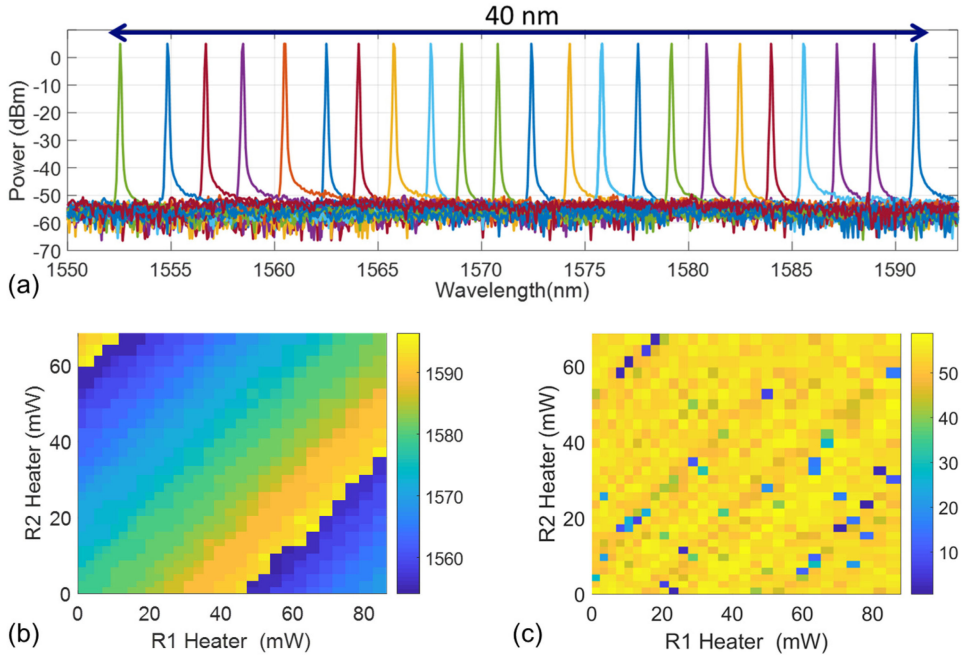

Fig. 10. (a) Course tuning spectra showing the tuning range (b) Two-dimensional wavelength tuning map of the dual-ring mirror laser. The color indicates the lasing wavelength in unit of nm. (c) Side-mode suppression ratio (SMSR) of the corresponding wavelength tuning map. The color indicates the SMSR values in dB scale.

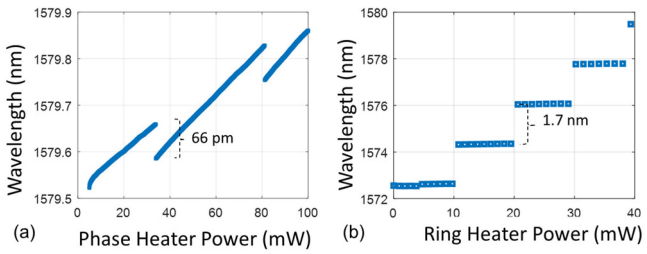

Fig. 11. Mode hopping behavior in the tunable laser (a) Mode-hops between two adjacent longitudinal modes by tuning the phase section (b) Mode-hops between two ring's modes by tuning one of the ring resonators.

(flicker) and *1/f*^{2} (random walk) frequency noise are dominant at the frequency range below 1 MHz. Also, some spikes corresponding to current source electronic noise and FM radio noise are also observed. A white noise floor of $S_F(f) = 65$ Hz^2/Hz level starts to be seen at an offset frequency of 35 MHz. This white noise level corresponds to a Schawlow-Townes linewidth of $\pi S_F(f) = 2.1$ kHz [40].

Fig. 12b plots the best linewidth measured when wavelength was tuned across the tuning range at the same pump current level. The linewidths are consistently about 2 kHz over the full span. This is close to the linewidth estimated by our model (Fig. 7b).

c) Detuned loading (optical negative feedback) effect: One property of our laser that is worth re-emphasizing here is the fact that the lowest linewidth is achieved when the lasing frequency is detuned to the low-frequency side of resonance, as shown previously in Fig. 7. The highest output power is obtained when the reflectivity on the back-mirror is maximized by aligning the lasing frequency to the resonance peak of the ring mirror. A direct implication of this is that the lowest linewidth operation point does not correspond to the highest output power operation point.

This detuned loading effect has been observed as shown in Fig. 13. The output power from our laser is split to two ports, one to a high resolution OSA (20 MHz resolution) and another to the laser noise measurement system, so that the lasing frequency and the frequency noise can be acquired simultaneously. At a fixed pump current of 120 mA to the gain region, we first tune the two ring resonators and the phase section to obtain the maximum output power (assisted by the on-chip photodiode) so that lasing is now occurring at the peak of the ring mirror's reflection resonance spectrum. We then start to change power to the heater on the phase section to detune the lasing frequency from the resonance peak. As we detune the lasing frequency to the positive side (up to $+1$ GHz), the frequency noise of the laser rapidly increased. In contrast, as we detune to the negative side (down to -4 GHz), the frequency gradually decreases to a certain point before starting to turn back. The frequency noise spectra are plotted all together in Fig. 13a. The extracted Lorentzian linewidths are plotted together with the output power as a function of the detuned frequency in Fig. 13. The detune frequency dependence of the measured Lorentzian linewidth matches quite well with the theoretical curve (the dash-line curve) that we calculated previously (Fig. 7b). At zero detuning, the output power of the laser is maximized, and the linewidth is about 4 kHz, about two times the minimum achievable linewidth.

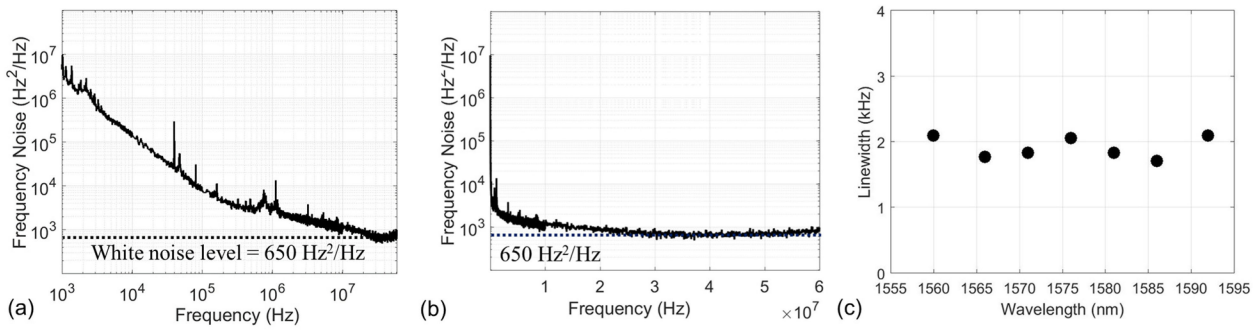

Fig. 12. (a) Frequency noise spectrum of the fabricated dual-ring mirror laser measured at 120 mA. (b) Frequency noise spectrum in linear scale to clearly show the white noise level (c) Best linewidth measured at wavelengths across the tuning range.

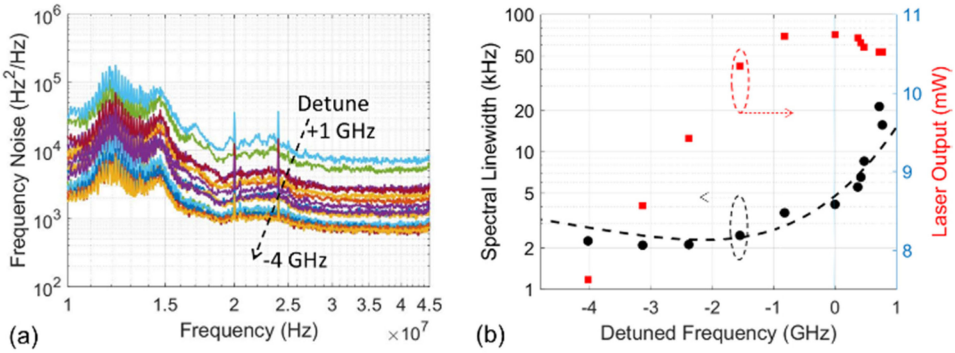

Fig. 13. (a) Frequency noise spectra of the dual-ring mirror laser when the lasing frequency is detuned away from resonance peak (b) Laser output power and the extracted linewidth from frequency noise measurement as functions of the detuned frequency. The dash-line show the theoretical curve calculated from Equation 11.

B. Generation 2: Hundreds Hz Level Spectral Linewidth Lasers

In this section, we describe the realization of the second generation of the tunable lasers with intrinsic linewidth of hundreds of Hz level, an order of magnitude improvement compared to the first-generation lasers that we showed above. The key to this linewidth level is the implementation of ultra-low loss silicon waveguides and extended cavity length with high single-mode selectivity from the use of novel multiple (>2) microresonator based laser cavity designs [21, 22]. These waveguides are extremely shallow rib waveguides, with only 56 nm etched out of the 500 nm of silicon. The waveguide geometry, fabrication and its integration into the heterogeneous Si/III-V photonic platform are detailed in our previous publication [22]. Here, we utilize the ultra-low loss waveguides to realize ring resonator mirrors for the lasers.

1) Gen. 2 Laser Designs: The structure of the laser mirror using three large radius rings within a Sagnac loop is shown in Fig. 14. The inclusion of three, and in some cases four, rings in the laser mirror design provides significant freedom in designing the performance parameters of the mirror, including high reflectivity, narrow bandwidth, and very high sidemode selectivity, e.g., 10 dB, over an ultra-wide wavelength tuning range, e.g., 120 nm.

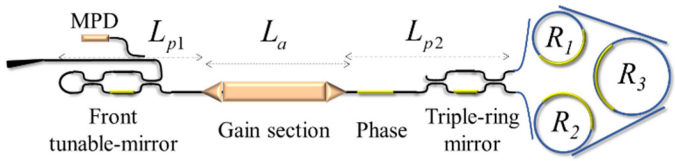

Fig. 14. Schematic of the triple-ring mirror based tunable laser. The front-mirror is a tunable-mirror formed with an MZI tunable directional coupler. The gain section is an optical amplifier heterogeneous Si/III-V waveguide, connected to the Si passive waveguides via two Si/III-V tapers. The back-mirror is a multiring mirror with three rings and a tunable coupler. 231 nm etch Si waveguides are drawn in black while 56 nm etch Si waveguides are in blue.

Key components are listed below:

Front tunable-mirror (low reflective mirror): The front-side loop mirror is formed by looping the two ports of a tunable MZI directional coupler. Since the reflectivity is adjustable for any wavelength, we can achieve the optimal reflectivity over the whole ∼120 nm span. The rib Si waveguide is 231 nm etched from the 500 nm thick Si layer.

An optical amplifier Si/III-V waveguide (gain section): We keep the same design of the amplifier waveguides used previously but the length of this active element is made longer (2.5 mm) than that of the first generation lasers to provide

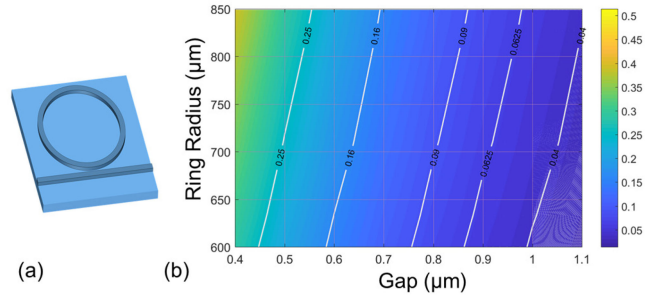

Fig. 15. (a) Schematic of the ring-bus coupler structure for simulation. (b) Power cross coupling ratio as a function of the ring radius and the gap between the ring and bus waveguide.

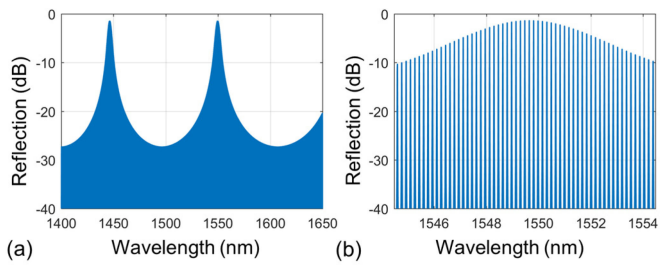

Fig. 16. Reflection spectrum of dual-ring mirror structure with large bend radii (~600 μm) shows low side mode suppression ratio. Plot (b) is the close-up of (a) centered around 1550 nm.

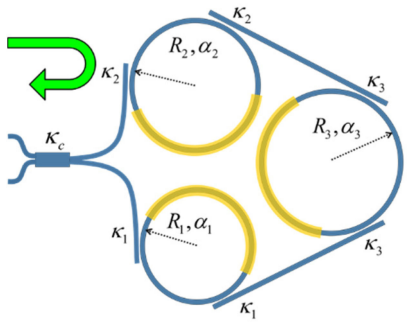

Fig. 17. Schematic configuration of triple-ring mirror used for the tunable lasers of Gen. 2.

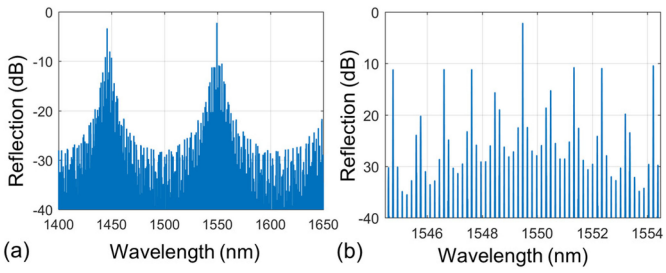

Fig. 18. Reflection spectra of the triple-ring mirror (a) Broad wavelength response (b) Close-in spectrum shows the sidemodes near the central reflection resonance peak with SMSR >8 dB.

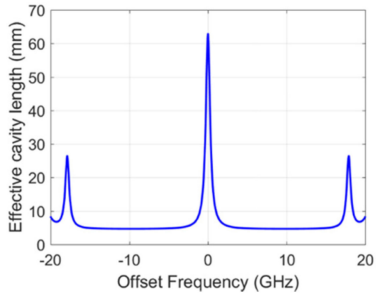

Fig. 19. Effective cavity length as a function of optical frequency offset from the resonance peak of the laser with the triple-ring mirror.

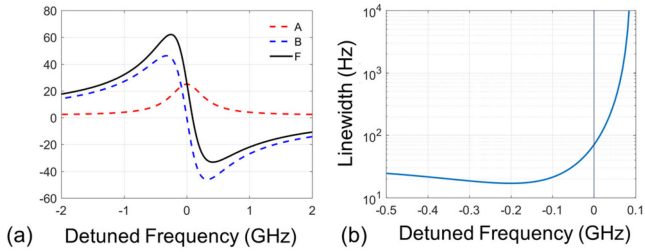

Fig. 20. Calculated values for coefficients A, B and F and estimated Lorentzian linewidth as functions of frequency detuned from the reflection peak resonance for a laser output power of 10 mW. Values of parameters used for these calculations are listed in Table I.

sufficient gain necessary for lasers with increased extended cavity loss due to the longer and more complex cavity design.

Multiring mirrors: The back-side mirror of the laser is a multiring mirror structure formed by a tunable coupler and three ring resonators, cascaded in a loop in add-drop configurations. The ring resonators are all 56 nm etched Si rib waveguides (therefore sketched in different color from the rest in Fig. 14). The designs of these multiring mirrors are the focus of the sub-sections that follow.

a) Ring resonators: The geometry of the ultra-low loss waveguides used for the ring resonators should be single mode for good laser operation. Based on the results in [22], a waveguide width of 1.8 μm and 56 nm etch-depth rib was chosen. With that geometry, the waveguide loss is about 0.16 dB/cm across the C+L bands and minimum bend radius is about 600 μm.

The coupling to the ring resonators is implemented with the simple configuration of a circular ring close to a straight bus waveguide, as shown in Fig. 15a. The power cross coupling ratio between the bus and the ring is simulated using the eigenmode expansion and CMT methods. A sweep of the two key parameters, ring radius and gap, were carried out to obtain a two-dimensional map shown in Fig. 15b. The map is convenient to look up for appropriate pairs of parameter values for desired coupling ratios.

b) Multiring mirrors: One immediate downside of the ultra-low loss waveguides is their large bend radius, which is almost 10x larger than that of the standard Si waveguides. The large radius results in a small FSR of the ring and renders the

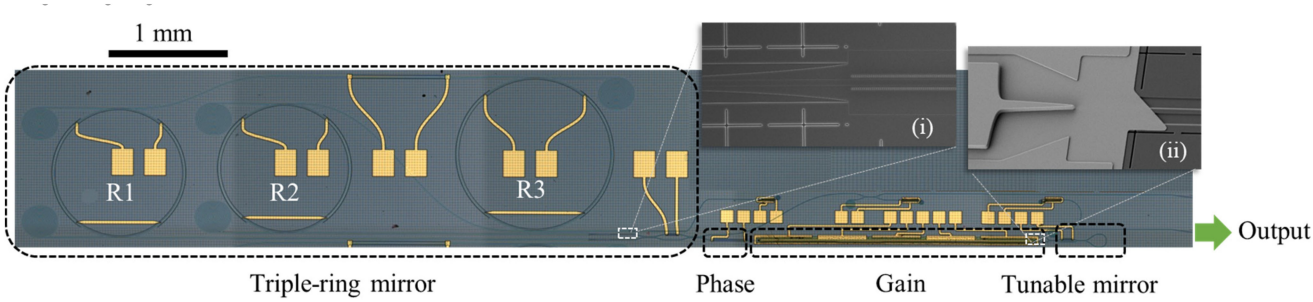

Fig. 21. Microscopic images of a fabricated triple-ring mirror laser. Microscopic images of a fabricated triple-ring mirror laser. (i) SEM image of a transition from 56 nm to 231 nm etched waveguides (ii) SEM image of a Si/III-V taper.

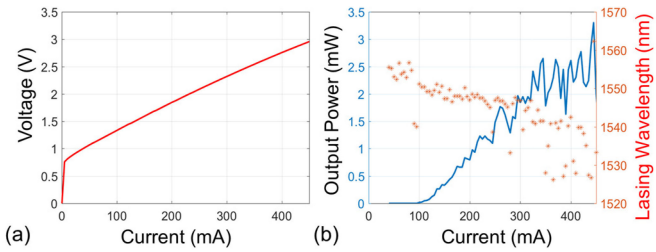

Fig. 22. (a) Current-voltage relation of the 2.5 mm long gain section (b) The light-current curve of the triple-ring laser. The lasing wavelength (right axis) was not constant across the current sweep due to thermal crosstalk.

dual-ring mirror incapable of providing sufficient side-mode-suppression-ratio (SMSR) for stable single mode lasing. To see this, Fig. 16 shows the simulated reflection spectrum of a dual-ring mirror with ring radii of 599.97 and 600.86 μm, and power coupling ratios all equal to 0.09. The spectrum is very dense when looking at a wide wavelength span due to the individual ring's FSR. When zooming in as in Fig. 16b, it is clear that there are many wavelengths for which the reflection is of similar value. That is not sufficient for a single frequency laser. However, the positives of the ultra-low loss waveguides with their large bend radius are the extended cavity lengths with low loss and narrow reflection bandwidth that they provide.

To take advantage of the ultra-low loss waveguides and long cavity lengths, additional rings are added to the laser mirror design [21]. A laser mirror with three ring resonators is illustrated in Fig. 17. The first ring radius is chosen to be close to the minimum bend radius at which the loss is not increased from that of straight waveguides, e.g., ~600 um. The second ring radius is typically chosen with a slightly larger radius, the value chosen to provide a large wavelength separation between the designed peak reflection (at 1550 nm) and the next reflection peak (one on the short wavelength side and one on the long wavelength side), which can also be called the superstructure period. In our case this was chosen to provide 120 nm of tuning range. In order to choose the radius of the third ring, and fourth (or higher number) ring if desired, computational analysis is required, as described in [22]. The proprietary simulation tool used for this analysis calculates all of the key laser mirror parameters for variations in the various ring radii, to provide the required laser mirror performance and additionally providing sufficient tolerance to small changes in each of the ring radii values that occur due to process fluctuations.

For the following spectral analysis, we use the analytical results for multiple ring mirrors described in Section II. Within each mirror, the power cross coupling ratios at all the ring resonators are chosen to be the same value (κ^2). The parameters for the triple-ring mirror are listed in Table I. The spectral responses of the triple-ring mirror are shown in Fig. 18, where a broad reflection spectrum and a close-in spectrum are plotted. The broad spectrum (Fig. 18a) shows a 114 nm superstructure period, while the close-in spectrum (Fig. 18b) reveals how effectively the third ring resonator helps suppress the sidemodes. In this case, an SMSR larger than 8dB over the whole tuning span is achieved, a substantial improvement from what is possible with only two Vernier rings (as in Fig. 16b). Parameters can be optimized for different tuning range, SMSR etc., based on the desired application; silicon nitride triple-ring and quad ring reflectors were previously demonstrated with SMSR >15 dB over > 45 nm of tuning range [41].

Fig. 19. plots the laser's effective cavity length calculated for the case of the triple-ring mirror, which adds over 50 mm of effective cavity length at resonance, which is much larger than the physical length of the rings' total circumference (~10 mm). This is an advantage of ring-resonators over Bragg gratings [42].

c) Laser linewidth: We applied the analysis in Section II again for laser linewidth study. The list of parameters is shown in Table I; most of these parameters are identical to what were used in Section II with changes highlighted in bold.

The estimated values of *A*, *B*, and *F* and the modified Schawlow-Townes linewidth as functions of the frequency detuning from the resonance peak frequency are then calculated with the output power assumed to be 10 mW. The predicted linewidth is below 100 Hz.

2) Gen. 2 Laser Fabrication: The designed laser is then fabricated in a modified version of the Si/III-V heterogeneous process. Some modification was necessary, including a self-aligned process for etching Si waveguides for zero-misalignment in the transition between 56 nm and 231 nm etch-depths, and a selective bonding process to preserve the ultra-low loss Si waveguide area throughout the entire process. The fabrication process flow can be found in [35], [42]. Stitched microscopic images of a completed device are shown in Fig. 21. Images of the self-aligned transition between the two types of Si waveguides and

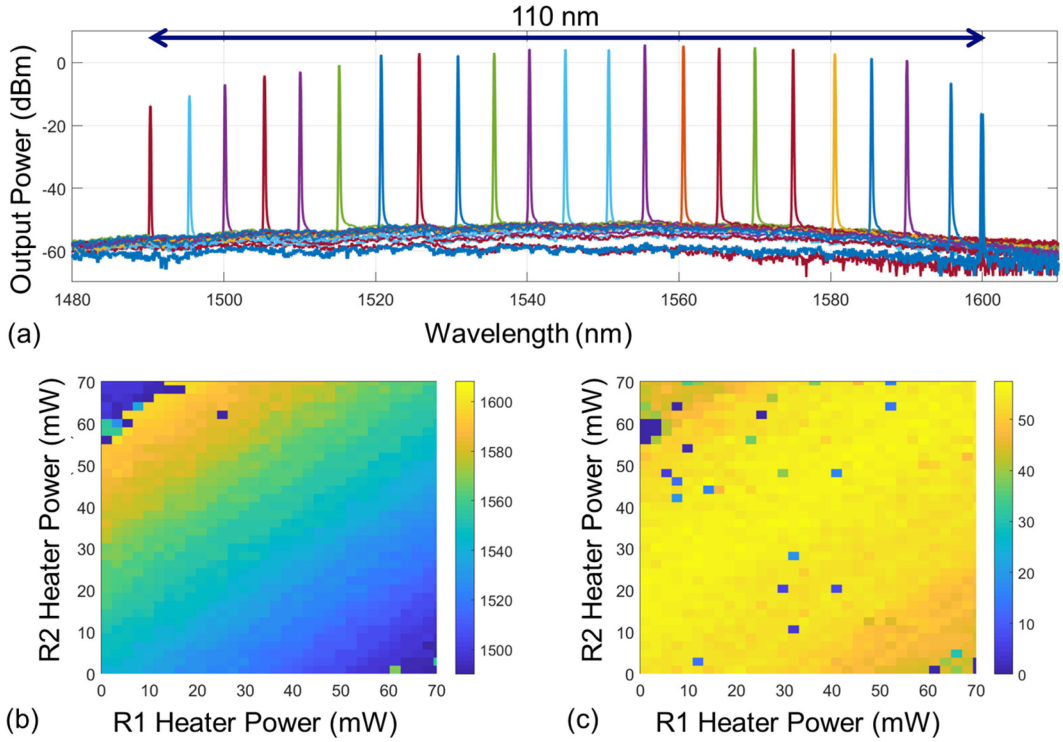

Fig. 23. Tuning characteristic of the triple-ring mirror laser: (a) Coarse tuning spectra showing the tuning range of 110 nm (b) Two-dimensional wavelength tuning map of the triple-ring mirror laser. The color indicates the lasing wavelength in units of nm. (c) Side-mode suppression ratio (SMSR) of the corresponding wavelength tuning map, showing >40 dB on most of the operation points.

Si/III-V taper are also shown in the insets *(i)* and *(ii)*. The facets of the lasers were mechanically polished for fiber coupling.

3) Gen. 2 Laser Characterization: The lasers were characterized with the same setup used for Gen. 1 in Section II. The current-voltage curve of the lasers is shown in Fig. 22a, while the current-output power curve for the triple-ring mirror laser is shown in Fig. 22b. The right y-axis in Fig. 22b shows the lasing wavelength at each current point. At each point the rings and phase section were tuned to obtain the maximum power, however, the lasing wavelength shifted quite a bit due to thermal crosstalk between the active sections and the rings, resulting in the non-smooth L-I curve. The laser's threshold current was about 100 mA. The max output power was only ∼3 mW, which is ∼3.3 times lower than the values used for the linewidth calculations in the previous section. This indicates that the total cavity loss is higher than expected, possibly due to fabrication imperfections in the III-V/Si taper, which was observed.

a) Gen. 2 laser wavelength tuning: We tested the laser wavelength tuning at a fixed injection current of 300 mA (∼3× threshold current) to the gain section of the laser. An initial coarse wavelength sweep was done to acquire the lasing spectra across the tuning range and followed by a two-dimensional sweep of ring heaters to obtain the full tuning map for the laser. In our test procedure, the electrical powers applied to the heaters on top of the smaller radii resonators are stepped. For each operation point, the power applied to the heaters on top of the third ring, phase section and tunable couplers were tuned to achieve the maximum output power indicated by the on-chip monitor photodiode. Because of thermal crosstalk between elements, it was necessary to run several tuning optimization cycles for each operation point. The measurement was automated by a computer program. The optimized lasing spectra at each operating point was recorded and post-processed for our analysis.

Results for the triple-ring mirror laser are shown in Fig. 23. The coarse tuning in Fig. 23a shows a 110 nm wide wavelength tuning from 1490 nm to 1600 nm. This agrees with the designed superstructure period of 114 nm. A linear and smooth 2D wavelength tuning map is achieved, as shown in Fig. 23b. The corresponding SMSR map is shown in Fig. 23c. SMSRs on almost all of lasing points are within the range 40 to 55 dB, even at wavelengths far off from the gain spectrum peak (∼1550 nm).

b) Gen. 2 laser frequency noise and linewidth: We measured the laser frequency noise to find the Lorentzian linewidth. The triple-ring mirror laser was measured with a Sycatus/Ogmentum phase noise measurement system [43], which has 20 MHz bandwidth, and the results are shown in Figure. 26. The measurement was taken at 300 mA pump current and slightly detuned from the peak resonance of 1545 nm wavelength.

Despite using all battery powered current sources isolated from power lines, there is still significant contribution to the measurement from other sources in the 10 kHz to 10 MHz range. The frequency noise spectrum seems to have not fully reached its white noise level within the 20 MHz measurement bandwidth of the instrument. Therefore, we deem 70 Hz^2/Hz as the upper-bound of the laser's white noise level. It is equivalent to state that the Lorentzian linewidth of the fabricated triple-ring

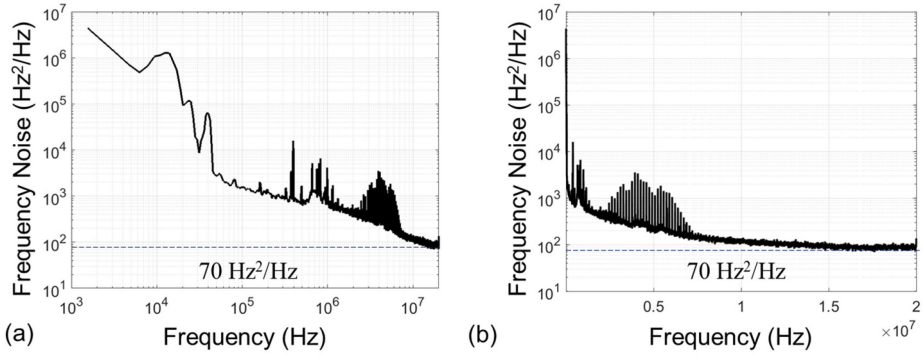

Fig. 24. (a) Frequency noise spectrum of the fabricated triple-ring mirror laser measured at 300 mA. (b) The same spectrum plotted with x-axis in linear scale to zoom-in on the noise at high frequency range. An upper bound of 70 Hz^2/Hz for the white noise level is drawn.

mirror is lower than 220 Hz [40]. This is a record low linewidth for any fully integrated laser reported in literature so far.

IV. Conclusion

This paper described the design, fabrication and characterization of narrow-linewidth lasers with wide wavelength tunability, an important class of semiconductor lasers for systems such as LIDAR, microwave photonics, and coherent communications. The first-generation lasers using a dual-ring mirror in standard silicon rib waveguides with propagation loss ∼1.2 dB/cm demonstrate 40 nm wavelength tuning range in C+L bands and Lorentzian linewidth ∼2 kHz. We experimentally verified the detuning loading (optical negative feedback) phenomenon in the laser operation, showing the lowest linewidth is achieved when the laser is red-detuned with respect to the peak reflection wavelength.

The second-generation lasers with a triple-ring mirror using ultra-low loss silicon waveguides with loss ∼0.16 dB/cm achieved record Lorentzian linewidth <220 Hz and an ultrawide tuning range of 110 nm across S+C+L bands. This unprecedented performance shows the clear potential for heterogeneous silicon photonics to realize low cost and highly scalable solution for many applications where the use of conventional lasers is prohibitive due to performance, high cost or size.

Since the lasers, especially Gen. 2, contain many elements from actives to passives and tapers, every improvement in those individual components would help to enhance the laser performances. Some future directions for improvement include:

- Optical amplifier (for the gain section of the lasers): The gain epi design used in this thesis was a result of multiple iterations of epi optimization [35]. However, there is still room for epi design optimization. For example, increase the strain in the quantum well would potentially help reduce the internal loss, which would benefit the linewidth. Furthermore, using a properly designed GRIN-SCHs [44] instead of abrupt SCHs as in the current lasers would increase the current injection efficiency for higher laser output power. For broad gain spectrum which is preferred for the ultrawide tuning range as in Gen. 2 lasers, variable-composition multi-quantum wells with different bandgaps can be used to obtain ultrabroad gain spectra [45], [46].
- Silicon waveguide loss: Since the propagation loss in the ultralow silicon waveguides is still mostly limited by scattering loss, improvement in waveguide line edge and sidewall roughness would significantly bring the loss down. Some highly effective methods have been known from literature such as photoresist reflow [47], [48] and oxidation smoothening [49], [50]. These techniques can be applied in future work to reduce the scattering loss, which could lead to significant improvement in the associated laser linewidth.
- Ring-resonators tuning: The present lasers utilize the thermo-refractive effect for wavelength tuning and to optimize lasing operation. Although this tuning mechanism is quite efficient due to the relatively high thermo-refractive coefficient in silicon, the switching time is slow and the thermal crosstalk between ring resonators does complicate the operation of the lasers. To completely overcome this issue, incorporation of other phase tuning mechanisms into rings could be pursued, such as piezoelectrics as in [51] and electro-optics as in [52]. Other areas of future work include laser frequency stabilization through external control circuits.

Acknowledgment

The authors would like to give special acknowledgments to C. Morton and J. Khurgin from Morton Photonics, J. Peters, S. Liu, P. Pintus, L. Liang, and M. Davenport from UCSB for their significant assistances in the success of the project. The authors also thank Sycatus/Ogmentum for lending the measurement tool. M. Tran thanks C. Santis at Caltech for insightful discussions on semiconductor laser phase noise.

The views and conclusions contained in this paper are those of the authors and should not be interpreted as presenting the official policies or position, either expressed or implied, of DARPA or the U.S. Government. Citation of manufacturer's or trade names does not constitute an official endorsement or approval of the use thereof. The U.S. Government is authorized to reproduce and distribute reprints for Government purposes notwithstanding any copyright notation hereon.

REFERENCES

[1] J. Geng, C. Spiegelberg, S. Jiang, and A. Abstract, "Narrow linewidth fiber laser for 100-km optical frequency domain reflectometry," *IEEE Photon. Technol. Lett.*, vol. 17, no. 9, pp. 1827–1829, Sep. 2005.

[2] S. L. I. Olsson *et al.*, "Probabilistically shaped PDM 4096-QAM transmission over up to 200 km of fiber using standard intradyne detection," *Opt. Express*, vol. 26, no. 4, pp. 4522–4530, 2018.

[3] Z. L. Newman *et al.*, "Architecture for the photonic integration of an optical atomic clock," Optica 6, pp. 680–685 2019.

[4] D. T. Spencer *et al.*, "An optical-frequency synthesizer using integrated photonics," *Nature*, vol. 557, no. 7703, pp. 81–85, 2018.

[5] Q.-F. Yang *et al.*, "Vernier spectrometer using counterpropagating soliton microcombs," *Science*, vol. 363, no. 6430, pp. 965–968, Mar. 2019.

[6] M. Fleming and A. Mooradian, "Spectral characteristics of external-cavity controlled semiconductor lasers," *IEEE J. Quantum Electron.*, vol. QE-17, no. 1, pp. 44–59, Jan. 1981.

[7] R. Wyatt, "Spectral linewidth of external cavity semiconductor lasers with strong, frequency-selective feedback," *Electron. Lett.*, vol. 21, no. 15, pp. 658–659, 1985.

[8] N. A. Olsson, C. H. Henry, R. F. Kazarinov, H. J. Lee, and B. H. Johnson, "Relation between chirp and linewidth reduction in external Bragg reflector semiconductor lasers," *Appl. Phys. Lett.*, vol. 51, no. 2, pp. 92–93, 1987.

[9] M. G. Littman and H. J. Metcalf, "Spectrally narrow pulsed dye laser without beam expander," *Appl. Opt.*, vol. 17, no. 14, pp. 2224–2227, Jul. 1978.

[10] W. Liang *et al.*, "Ultralow noise miniature external cavity semiconductor laser," *Nat. Commun.*, vol. 6, 2015, Art. no. 7371.

[11] P. A. Morton and M. J. Morton, "High-power, ultra-low noise hybrid lasers for microwave photonics and optical sensing," *J. Light. Technol.*, vol. 36, no. 21, pp. 5048–5057, Nov. 2018.

[12] A. Verdier *et al.*, "Ultrawideband wavelength-tunable hybrid external-cavity lasers," *J. Light. Technol.*, vol. 36, no. 1, pp. 37–43, Jan. 2018.

[13] Y. Fan *et al.*, "290 Hz intrinsic linewidth from an integrated optical chip-based widely tunable in P-Si3N4 hybrid Laser," presented at the Conf. Lasers Electro-Opt., 2017, Paper JTh5C.9.

[14] B. Stern, X. Ji, A. Dutt, and M. Lipson, "Compact narrow-linewidth integrated laser based on a low-loss silicon nitride ring resonator," *Opt. Lett.*, vol. 42, no. 21, pp. 4541–4544, 2017.

[15] C. Xiang, P. A. Morton, and J. E. Bowers, "Ultra-narrow linewidth laser based on a semiconductor gain chip and extended Si_3N_4 Bragg grating," *Opt. Lett.*, vol. 44, no. 15, pp. 3825–3828, Aug. 2019.

[16] N. Kobayashi *et al.*, "Silicon photonic hybrid ring-filter external cavity wavelength tunable lasers," *J. Lightw. Technol.*, vol. 33, no. 6, pp. 1241–1246, Mar. 2015.

[17] H. Guan *et al.*, "Widely-tunable, narrow-linewidth III-V/silicon hybrid external-cavity laser for coherent communication," *Opt. Express*, vol. 26, no. 7, pp. 7920–7933, 2018.

[18] R. Jones *et al.*, "Heterogeneously integrated InP/silicon photonics: Fabricating fully functional transceivers," *IEEE Nanotechnol. Mag.*, vol. 13, no. 2, pp. 17–26, Apr. 2019.

[19] T. Komljenovic *et al.*, "Photonic integrated circuits using heterogeneous integration on silicon," *Proc. IEEE*, vol. 106, no. 12, pp. 2246–2257, Dec. 2018.

[20] B. Liu, A. Shakouri, and J. E. Bowers, "Passive microring-resonator-coupled lasers," *Appl. Phys. Lett.*, vol. 79, no. 22, pp. 3561–3563, 2001.

[21] T. Komljenovic and J. E. Bowers, "Monolithically integrated high-Q rings for narrow linewidth widely tunable lasers," *IEEE J. Quantum Electron.*, vol. 51, no. 11, Nov. 2015, Art. no. 0600610.

[22] M. Tran *et al.*, "Ultra-low-loss silicon waveguides for heterogeneously integrated silicon/III-V photonics," *Appl. Sci.*, vol. 8, no. 7, 2018, Art. no. 1139.

[23] P. Morton and J. Khurgin, "Low noise, high power, multiple-microresonator based laser," U.S. Patent 9, 559, 484, Jan. 31, 2017.

[24] P. Morton, J. Khurgin, and C. Morton, "Multiple-microresonator based laser," U.S. Patent 9748726, Aug. 29, 2017.

[25] K. Kikuchi, "Effect of 1/f-type FM noise on semiconductor-laser linewidth residual in high-power limit," *IEEE J. Quantum Electron.*, vol. 25, no. 4, pp. 684–688, Apr. 1989.

[26] M. L. Davenport *et al.*, "Heterogeneous silicon/III-V semiconductor optical amplifiers," *IEEE J. Sel. Top. Quantum Electron.*, vol. 22, no. 6, Nov./Dec. 2016, Art. no. 3100111.

[27] M. L. Davenport, M. A. Tran, T. Komljenovic, and J. E. Bowers, "Heterogeneous integration of III–V lasers on Si by bonding," *Semicond. Semimetals*, vol. 99, pp. 139–188, Jan. 2018.

[28] L. Coldren, S. Corzine, and M. Mashanovitch, *Diode Lasers and Photonic Integrated Circuits*, 2nd ed. Hoboken, NJ, USA: Wiley, 2012.

[29] E. Patzak, A. Sugimura, S. Saito, T. Mukai, and H. Olesen, "Semiconductor laser linewidth in optical feedback configurations," *Electron. Lett.*, vol. 19, no. 24, pp. 1026–1027, Nov. 1983.

[30] R. F. Kazarinov and C. H. Henry, "The relation of line narrowing and chirp reduction resulting from the coupling of a semiconductor laser to a passive resonator," *IEEE J. Quantum Electron.*, vol. QE-23, no. 9, pp. 1401–1409, Sep. 1987.

[31] C. T. Santis, Y. Vilenchik, N. Satyan, G. Rakuljic, and A. Yariv, "Quantum control of phase fluctuations in semiconductor lasers," *Proc. Nat. Acad. Sci.*, vol. 115, no. 34, pp. E7896–E7904, 2018.

[32] C. T. Santis, S. T. Steger, Y. Vilenchik, A. Vasilyev, and A. Yariv, "High-coherence semiconductor lasers based on integral high-Q resonators in hybrid Si/III-V platforms," *Proc. Nat. Acad. Sci.*, vol. 111, no. 8, pp. 2879–2884, 2014.

[33] K. Vahala and A. Yariv, "Detuned loading in coupled cavity semiconductor lasers—Effect on quantum noise and dynamics," *Appl. Phys. Lett.*, vol. 45, no. 5, pp. 501–503, 1984.

[34] M. Osinski and J. Buus, "Papers linewidth broadening factor in semiconductor lasers-an overview," *IEEE J. Quantum Electron.*, vol. QE-23, no. 1, pp. 9–29, Jan. 1987.

[35] M. L. Davenport, "Heterogeneous silicon III-V mode-locked lasers," Ph.D. dissertation, Dept. Elect. Comput. Eng., Univ. California, Santa Barbara, Santa Barbara, CA, USA, 2017.

[36] D. Huang *et al.*, "Sub-kHz linewidth extended-DBR lasers heterogeneously integrated on silicon," presented at the Opt. Fiber Commun. Conf., 2019, Paper W4E.4.

[37] T. Okoshi, K. Kikuchi, and A. Nakayama, "Novel method for high resolution measurement of laser output spectrum," *Electron. Lett.*, vol. 16, no. 16, pp. 630–631, 1980.

[38] L. B. Mercer, "1/f frequency noise effects on self-heterodyne linewidth measurements," *J. Lightw. Technol.*, vol. 9, no. 4, pp. 485–493, 1991.

[39] "HI-Q Optical TMS | OEwaves," [Online]. Available: https://oewaves.com/hi-q-optical-tms. Accessed: Mar. 13, 2019.

[40] K. Kikuchi and T. Okoshi, "Estimation of linewidth enhancement factor of algaas lasers by correlation measurement between FM and AM noises," *IEEE J. Quantum Electron.*, vol. QE-21, no. 6, pp. 669–673, Jun. 1985.

[41] C. Xiang, P. A. Morton, J. Khurgin, C. Morton, and J. E. Bowers, "Widely tunable Si3N4 riple-ring and quad-ring resonator laser reflectors and filters," in *Proc. IEEE 15th Int. Conf. Group IV Photon.*, 2018, pp. 1–2.

[42] D. Huang *et al.*, "High-power sub-kHz linewidth lasers fully integrated on silicon," *Optica*, vol. 6, no. 6, 2019, Art. no. 745.

[43] "Optical noise analyzer," [Online]. Available: http://www.sycatus.com/en/products/ona/. [Accessed: 17-Mar-2019].

[44] H. Hirayama, Y. Miyake, and M. Asada, "Analysis of current injection efficiency of separate-confinement-heterostructure quantum-film lasers," *IEEE J. Quantum Electron.*, vol. 28, no. 1, pp. 68–74, Jan. 1992.

[45] I. J. Fritz, J. F. Klem, M. J. Hafich, A. J. Howard, and H. P. Hjalmarson, "Broad-band light-emitting diode for 1.4-2.0 μm using variable-composition InGaAs quantum wells," *IEEE Photon. Technol. Lett.*, vol. 7, no. 11, pp. 1270–1272, Nov. 1995.

[46] X. Zhu *et al.*, "1.4-μm InGaAsP-InP strained multiple-quantum-well laser for broad-wavelength tunability," *IEEE Photon. Technol. Lett.*, vol. 9, no. 9, pp. 1202–1204, Sep. 1997.

[47] J. CAI, P. H. LIM, Y. Ishikawa, and K. WADA, "Silicon waveguide sidewall smoothing by resist reflowing," *J. Nonlinear Opt. Phys. Mater.*, vol. 19, no. 04, pp. 801–809, 2010.

[48] G. A. Porkolab, P. Apiratikul, B. Wang, S. H. Guo, and C. J. K. Richardson, "Low propagation loss AlGaAs waveguides fabricated with plasma-assisted photoresist reflow," *Opt. Express*, vol. 22, no. 7, pp. 7733–7743, 2014.

[49] K. K. Lee, D. R. Lim, L. C. Kimerling, J. Shin, and F. Cerrina, "Fabrication of ultralow-loss Si/SiO(2) waveguides by roughness reduction," *Opt. Lett.*, vol. 26, no. 23, pp. 1888–1890, 2001.

[50] D. K. Sparacin, S. J. Spector, and L. C. Kimerling, "Silicon waveguide sidewall smoothing by wet chemical oxidation," *J. Light. Technol.*, vol. 23, no. 8, pp. 2455–2461, Aug. 2005.

[51] W. Jin, R. G. Polcawich, P. A. Morton, and J. E. Bowers, "Phase tuning by length contraction," *Opt. Express*, vol. 26, no. 3, pp. 3174–3187, Feb. 2018.

[52] M. He *et al.*, "High-performance hybrid silicon and lithium niobate Mach–Zehnder modulators for 100 Gbit s^{-1} and beyond," *Nat. Photon.*, vol. 13, no. 5, pp. 359–364, May 2019.

Minh A. Tran received the B.S. degree in electrical engineering from the University of Tokyo, Tokyo, Japan, in 2013, and the M.S. and Ph.D. degrees in electrical engineering from the University of California, Santa Barbara, Santa Barbara, CA, USA, in 2015 and 2019 respectively. He is currently with Nexus Photonics, LLC, Santa Barbara, CA, USA.

Duanni Huang received the B.S. degree in electrical engineering from the Massachusetts Institute of Technology, Cambridge, MA, USA, in 2013, and the M.S. and Ph.D. degrees in electrical engineering from the University of California, Santa Barbara, Santa Barbara, CA, USA in 2015 and 2019 respectively. He is currently a Research Scientist with Intel Labs, working on silicon photonics. His current research focuses on silicon photonics with an emphasis on heterogenous integration.

Joel Guo received the B.S. degree in electrical engineering from the University of Texas at Austin, Austin, TX, USA, in 2018. He is currently working toward the Ph.D. degree in electrical engineering with the Bowers group. His current research involves narrow linewidth and high-power lasers heterogenously integrated on silicon.

Tin Komljenovic received the M.Sc. and Ph.D. degrees in electrical engineering from the Faculty of Electrical Engineering and Computing, University of Zagreb, Zagreb, Croatia, in 2007 and 2012, respectively. During his Ph.D. studies, he was a Visiting Researcher at IETR, University of Rennes, Rennes, France. He cofounded Nexus Photonics, LLC, where he currently the CEO. He has authored or coauthored more than 70 papers and seven patents. His current research interests include integrated photonic circuits, tunable optical sources, and LIDAR. He is a recipient of the EuMA young scientist prize and the Marie Curie FP7 grant.

Paul A. Morton received the B.Sc., M.Eng., and Ph.D. degrees in electrical engineering from the University of Bath, Bath, U.K. He was a Postdoctoral Researcher with the University of California, Santa Barbara, before becoming a Member of Technical Staff with the AT&T Bell Laboratories, Murray Hill, NJ, USA, where he made fundamental research contributions in the areas of high-speed laser diodes, mode-locked optical pulse sources, and photonic integration. At CIENA, he was a technical leader in the development of commercial high-capacity Dense Wavelength Division Multiplexing (DWDM) transmission and switching systems. He co-founded Morton Photonics, which develops photonic components, photonic-integrated circuits on the silicon photonics platform utilizing heterogenous integration, and subsystems based on these devices, for applications of high-performance analog RF photonic links, LIDAR, 5G systems, optical sensing, and photonic processing for phased array sensors. He has authored or coauthred two book chapters, more than 100 journal and conference papers, and holds 16 patents. He is a Fellow of the Optical Society of America.

John E. Bowers received the M.S. and Ph.D. degrees from Stanford University, Stanford, CA, USA. Before joining University of California, Santa Barbara (UCSB), Santa Barbara, CA, USA, he was with AT& Bell Laboratories and Honeywell. He holds the Fred Kavli Chair in Nanotechnology, and is the Director of the Institute for Energy Efficiency and a Professor with the Departments of Electrical and Computer Engineering and Materials, UCSB. He is a cofounder of Aurrion, Aerius Photonics and Calient Networks. His research primarily focuses on silicon photonics and photonic-integrated circuits. He is a member of the National Academy of Engineering and a fellow of OSA and the American Physical Society. He is a recipient of the OSA/IEEE Tyndall Award, the OSA Holonyak Prize, the IEEE LEOS William Streifer Award, and the South Coast Business and Technology Entrepreneur of the Year Award. He and coworkers received the EE Times Annual Creativity in Electronics (ACE) Award for Most Promising Technology for the heterogeneous silicon laser in 2007.